

Supplementary Information

High capacity V-based metal hydride electrodes for rechargeable batteries

Heng Yang, Nicholas J. Weadock, Hongjin Tan, and Brent Fultz

California Institute of Technology, Pasadena, California 91125, USA

The microstructures of the $\text{Ti}_{29}\text{V}_{62-x}\text{Ni}_9\text{Cr}_x$ ($x = 0, 6, \text{ and } 12$) alloys were characterized by x-ray diffraction (XRD), scanning electron microscopy (SEM) with backscattered electron imaging (BES), and energy dispersive x-ray spectroscopy (EDS). Alloy samples characterized by XRD were pulverized to a fine powder via the procedures outlined in the main text. For SEM and EDS, the samples were mounted in graphite and polished to a mirror finish.

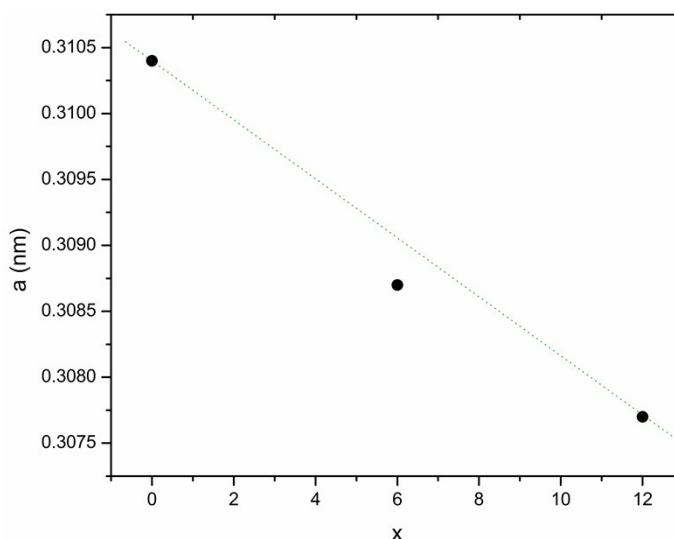


Fig. S1 Lattice parameter, a , of $\text{Ti}_{29}\text{V}_{62-x}\text{Ni}_9\text{Cr}_x$ ($x = 0, 6, \text{ and } 12$) alloys

Measuring the lattice parameter is challenging because of the broad, overlapping peaks from regions of the BCC phase with different chemical compositions. The lattice parameter, a , of the majority V-rich region clearly decreases with higher Cr content, however. From our analysis of the backscattered electron images, we estimate the fraction of the Ni-rich region to be about 9 vol%. The small amount of the Ni-rich region, the small number of reflections in the measured 2θ range, and the broad, overlapping peaks makes analysis of the lattice parameter of this region

difficult. Given that the second peak has nearly disappeared in the $x=12$ sample, we estimate that the lattice parameter of the Ni-rich region is slightly smaller, on the order of $0.3065 - 0.307$ nm.

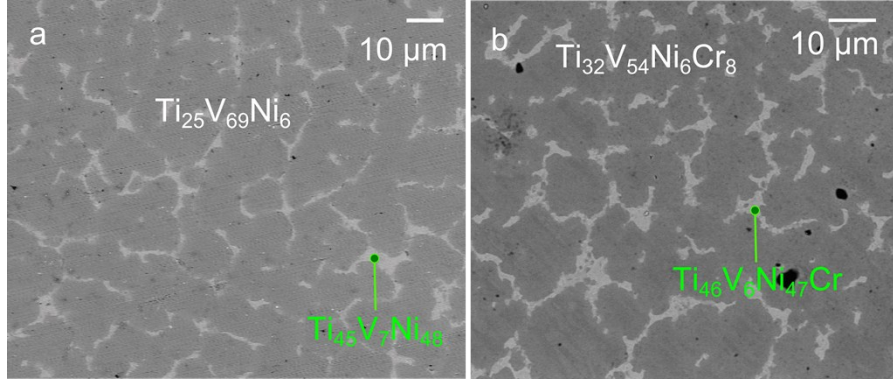


Fig. S2 SEM images and EDS results of (a) Ti₂₉V₆₂Ni₉ and (b) Ti₂₉V₅₆Ni₉Cr₆ alloy ingots. The compositions reported are the average compositions of the V-rich (dark) and Ni-rich (light) regions as determined by EDS.

Electrochemical cells were assembled using electrodes of the Ti₂₉V_{62-x}Ni₉Cr_x ($x = 0, 6,$ and 12) alloys. Three types of cells were used: (1) 3-electrode beaker cells assembled in air, (2) a 3-electrode Ar purged cell, and (3) coin cells assembled in air. In addition to electrochemical cycling, elemental analysis of the electrolyte was performed with inductively coupled plasma mass spectrometry (ICP-MS), and the surface oxidation states of the cycled electrodes were characterized by x-ray photoelectron spectroscopy (XPS).

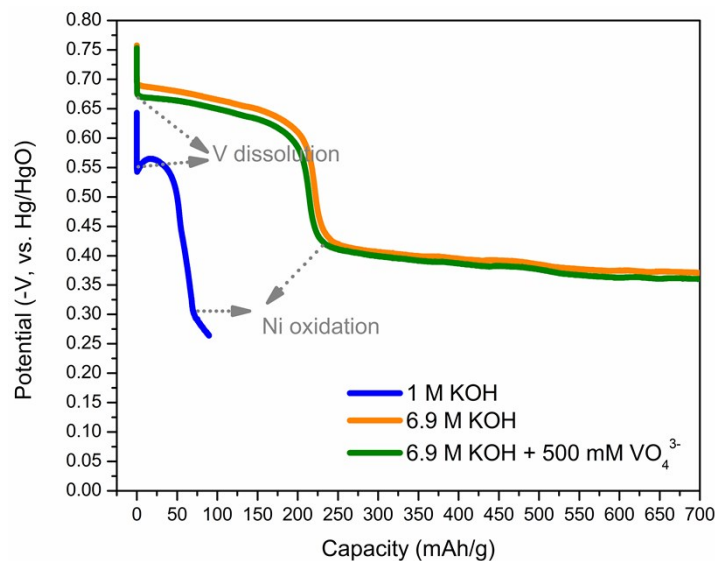


Fig. S3 Discharge curve of $\text{Ti}_{29}\text{V}_{62}\text{Ni}_9$ electrode in KOH solutions.

Figure S3 shows the discharge curves of $\text{Ti}_{29}\text{V}_{62}\text{Ni}_9$ electrodes in pristine 1 M KOH, 6.9 M KOH, and 6.9 M KOH with 500 mM KVO_3 . All three electrodes were assembled in air in three-electrode beaker cells. The Hg/HgO reference electrodes were prepared with the corresponding KOH solutions. The experiments were performed by discharging at a small current of 10 mA/g based on the loading of the alloy powder. These cells were discharged without prior charging, so the capacity is a result of metal oxidation rather than oxidation of absorbed hydrogen. According to the Pourbaix diagram, vanadium oxidation to vanadate ions is expected at around -0.9 V vs. Hg/HgO (pH =15) for a pure vanadium electrode. The corresponding dissolution potential for the alloy is approximately -0.7 V in 6.9 M KOH solution, consistent with that reported in the main text (Fig. 3a). Increasing the vanadate ion concentration in the electrolyte, or reducing the pH, both shift the dissolution potential to a more positive value, as predicted by the Pourbaix diagram. Slower kinetics may also contribute to the shift in dissolution potential, however.

Table S1 ICP-MS results of the KOH solutions in which $\text{Ti}_{29}\text{V}_{62-x}\text{Ni}_9\text{Cr}_x$ ($x = 0$ and 12) alloy electrodes were stored for 2 days.

Alloy composition	% Loss from electrode			
	Ti	V	Ni	Cr
$\text{Ti}_{29}\text{V}_{62}\text{Ni}_9$	0.04	6.77	0.11	-
$\text{Ti}_{29}\text{V}_{50}\text{Ni}_9\text{Cr}_{12}$	0.09	2.47	0.07	0.15

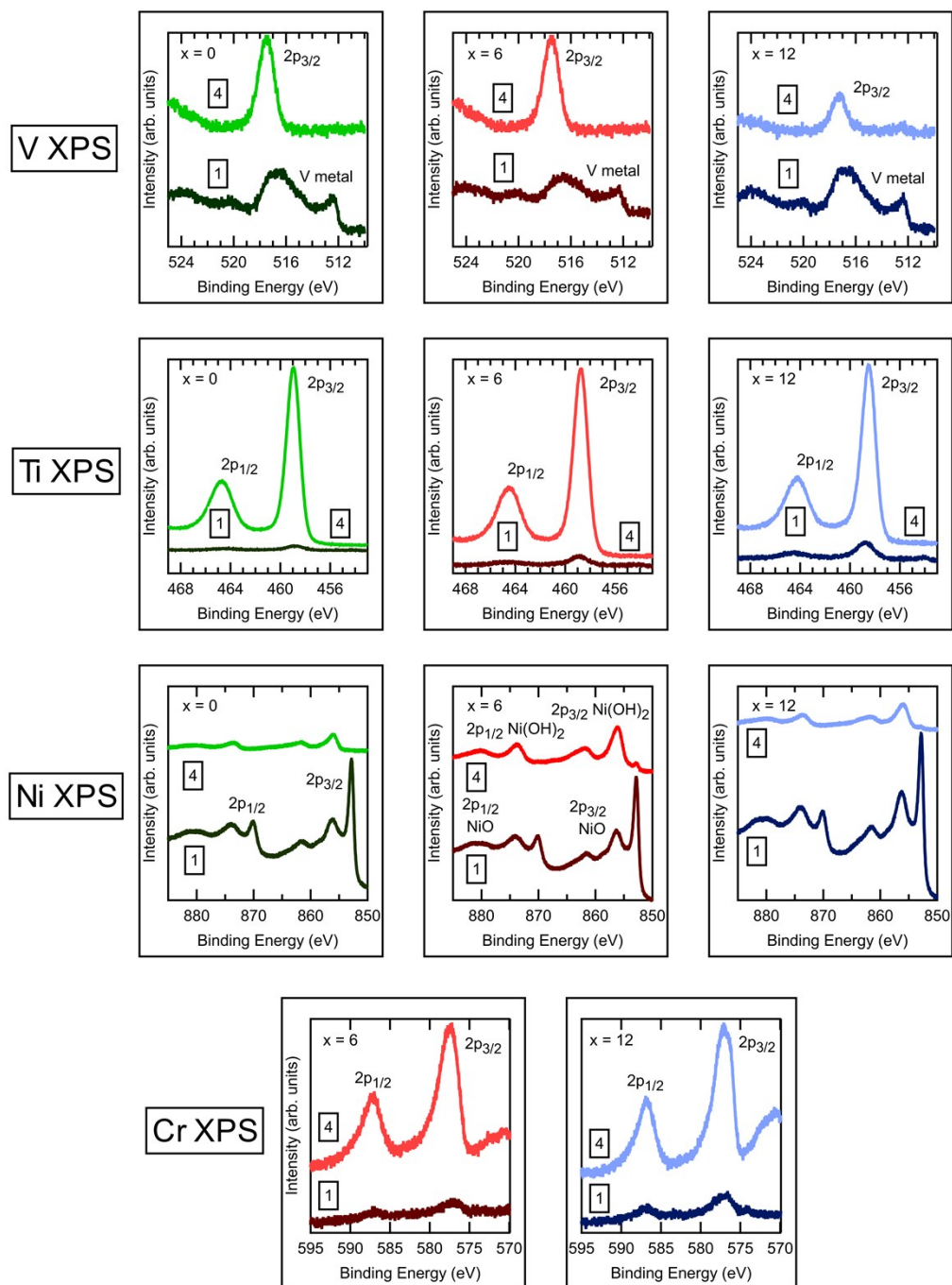


Fig. S4 XPS spectra of V, Cr, Ni, and Ti prior to charge and after full discharge of $\text{Ti}_{29}\text{V}_{62-x}\text{Ni}_9\text{Cr}_x$ ($x = 0, 6, \text{ and } 12$) alloys. Boxed numbers correspond to the state of charge indicated in the main text Fig. 3a.

The XPS spectra for the $\text{Ti}_{29}\text{V}_{62-x}\text{Ni}_9\text{Cr}_x$ ($x = 0, 6, 12$) electrodes before cycling (spectra [1]) and after charging and discharging to -0.50 V (spectra [4]) are presented in Fig. S4. The V $2p_{3/2}$ metallic peaks disappear for the $\text{Ti}_{29}\text{V}_{62}\text{Ni}_9$ and $\text{Ti}_{29}\text{V}_{56}\text{Ni}_9\text{Cr}_6$ electrodes, and the oxide $2p_{3/2}$ peaks shift to a higher binding energy. This shift corresponds to an increase in the oxidation state of the V. The surface oxide is likely a mixed oxide and manifests as a broad peak. There are no shifts in the Ti $2p_{3/2}$ or $2p_{1/2}$ peaks; the native oxide layer appears to be stable in the electrolyte environment. The XPS spectra for Ni show a disappearance of the metallic $2p_{3/2}$ and $2p_{1/2}$ peaks and emergence of the corresponding $\text{Ni}(\text{OH})_2$ peaks. The NiO $2p_{3/2}$ and $2p_{1/2}$ peaks persist during cycling. The broad Cr $2p_{3/2}$ and $2p_{1/2}$ peaks have a small shift to higher energy and an increase in amplitude, indicating that a CrO_x layer has formed on the surface. Similar to V, the CrO_x layer is likely a mixed oxide.

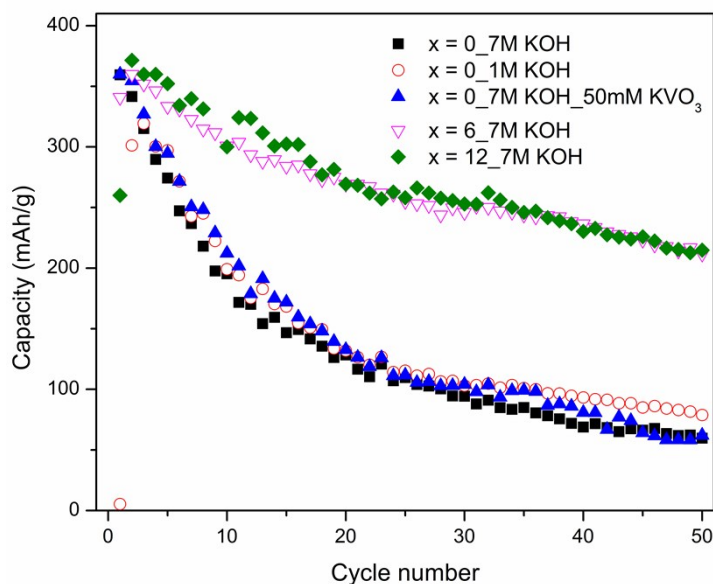


Fig. S5 Cycle performance of $\text{Ti}_{29}\text{V}_{62}\text{Ni}_9\text{Cr}_x$ ($x = 0, 6,$ and 12) alloy electrodes in various electrolytes. All tests were performed in air-saturated beaker cells. Cells were charged to 800 mAh/g, then discharged following the three-step procedure to -0.75 V.

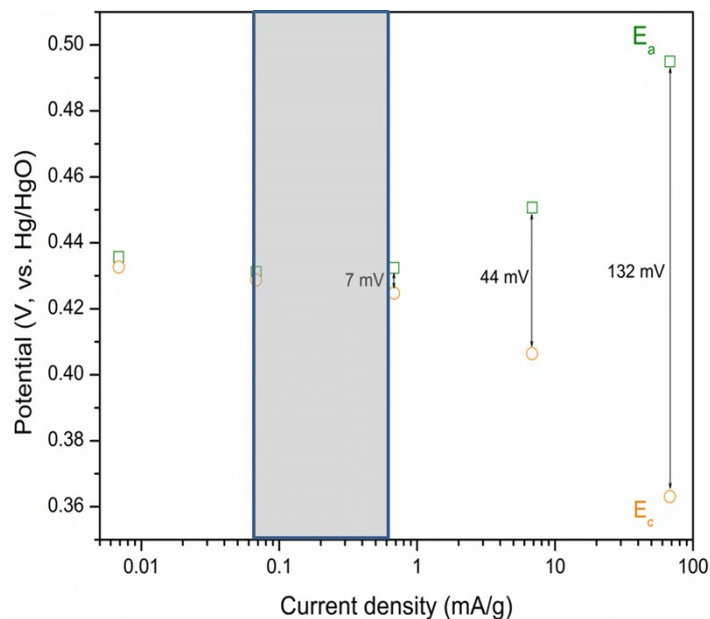


Fig. S6 Operation potential for the Ni(OH)₂/NiO(OH) electrode used for coin cell assembly. Current density is based on the mass loading of the Ni(OH)₂ electrode powder mixture. E_a and E_c correspond to the plateau potentials on charge and discharge, respectively. The shaded area corresponds to the applied current density range for the paired MH electrode (10 to 100 mA/g based on 3 mg/cm² loading).

The design of the coin cells considered the following factors: (1) with a small internal volume, the cells can be sealed in air with negligible amount of oxygen trapped inside the cells; (2) the MH electrode is paired with a much larger Ni(OH)₂ positive electrode, so that the positive electrode does not evolve oxygen during cell overcharge and the potential remain relatively stable as a reference electrode. This configuration is also more sensitive to capacity degradation of the MH electrode. Figure S6 shows the operation potential of the Ni(OH)₂/NiOOH electrode used in this study. These electrodes were obtained from BASF (BASF-Ovonic, Rochester Hills, MI, USA) and punched into disks with a 1.27 cm diameter. The capacity of each electrode is about 24 mAh. The results shown in Fig. S6 were obtained by first charging a Ni(OH)₂ electrode to 12 mAh, converting part of the Ni(OH)₂ to NiOOH. The Ni(OH)₂/NiOOH electrode was then charged at the specific current density shown in Fig. S6 for 7200 s, rested for 1200 s, and discharged at the same current density for 7200 s. The charge (E_a) and discharge (E_c) plateau potentials were recorded and plotted in Fig. S6. The smallest current for the discharge of the coin cells was 20

mA/g, and the vanadium dissolution potential for Cr-free alloy is at about -0.7 V versus Hg/HgO (Fig. S1 and Fig. 3a). For these reasons, and to allow a voltage window as large as possible, the cut-off voltage for all coin cells was set at 1.10 V. All coin cells were assembled with the half-charged cathodes.

The $\text{Ti}_{29}\text{V}_{50}\text{Ni}_9\text{Cr}_{12}$ electrodes in Fig. 5a, b were charged for 550 mAh/g, which is higher than its maximum discharge capacity as measured in Fig. 4. The Coulombic efficiency of these coin cells are also less than 100%. As a result, a small amount of hydrogen is evolved during charging, which may be consumed on the positive electrode by reducing $\text{NiO}(\text{OH})$ to $\text{Ni}(\text{OH})_2$.¹

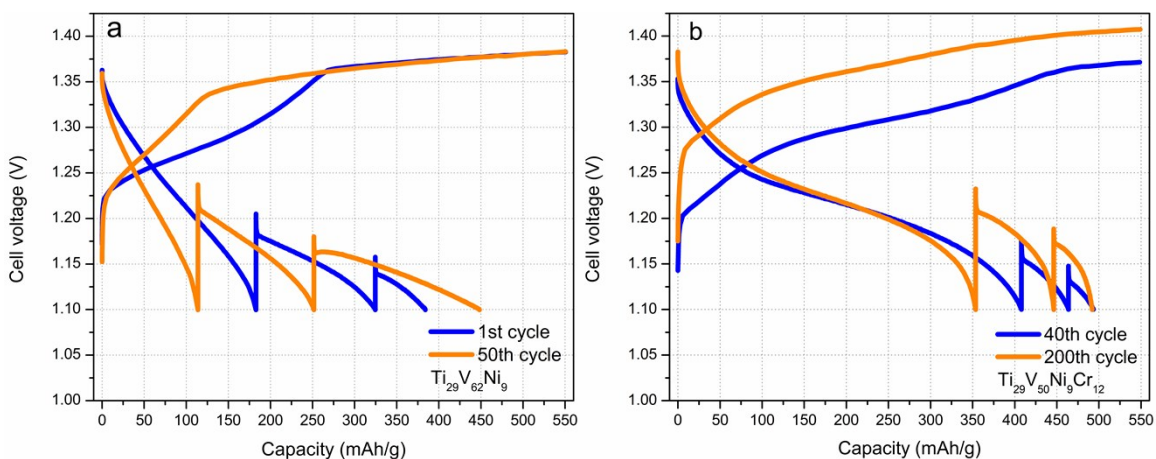


Fig. S7 Charge/discharge curves of $\text{Ti}_{29}\text{V}_{62}\text{Ni}_9$ and $\text{Ti}_{29}\text{V}_{50}\text{Ni}_9\text{Cr}_{12}$ electrodes in the coin cell configuration. The cells were charged for 550 mAh/g and three-step discharged at 100, 40 and 20 mA/g to 1.10 V. The decrease of discharge capacity at the high current step shows that the rate capability of the MH electrode decreases with cycling, despite excellent capacity retention.

Section 3: Energy density calculations of a MH-Air battery cell

Energy density calculations of the MH-air batteries are based on a prismatic cell design. This MH-air cell has three electrodes: oxygen-reduction-reaction (ORR) electrode, oxygen-evolution-reaction (OER) electrode, and a MH anode. The ORR electrode is a commercial alkaline fuel cell air electrode from Electric Fuel (Electric Fuel Limited, Bet Shemesh, Israel) with the catalytic

MnO₂ on a substrate film of PTFE.² The OER electrode is made from Monel mesh. The MH anode is made by pressing MH alloy powder onto a nickel mesh substrate. Figure S8 shows the layout of the two-sided prismatic cell. The cell consists of two ORR-MH-OER stacks with the OER electrodes facing the interior of the cell. The OER electrodes are separated by a channel through which electrolyte flows. Flowing electrolyte is utilized to compensate for local changes in electrolyte concentration and pH due to water loss or generation as the cell charges or discharges.

The cell was designed to achieve 100 Wh with an overall dimension of 20.2 cm x 10.2 cm x 1.13 cm. The cell discharge potential is determined from the ORR overpotential data as a function of cell current density, provided by the vendor of ORR electrode, and our cycling data for the MH anode. The air electrode potential is presented in Fig. S9. The current density needed from the ORR electrode is chosen to match the specifications of the MH anode for a given discharge rate. The total weight of the cell also includes those of passive components of electrode substrates, separators, frame, and seal materials. Key input parameters of this model are the MH anode thickness and MH anode specific discharge capacity. Other input parameters including dimension of the prismatic cell, dimensions of the two air electrodes, and the cell discharge C-rate, are preset based on project targets and some of the preliminary lab testing results.

Based on the preliminary experimental results of the cell similar to this design, the MH anode specific discharge capacity is in a range of 150 – 550 mAh/g, and the practical thickness of the anode is above 300 microns. The model varies the MH anode capacity from 0 – 800 mAh/g, and thickness from 0.3 – 5 mm. Varying these two parameters leads to a 2D contour plot of cell level gravimetric and volumetric energy density as shown in the main text Fig. 7. The colored lines are regions of constant energy density in Wh/kg or Wh/L. MH anodes containing Ti₂₉V_{62-x}Ni₉Cr_x ($x = 0, 6, 12$) were demonstrated in the manuscript to have a specific capacity of more than 400 mAh/g, making it possible to achieve 200 Wh/kg. From the sensitivity analysis of Fig. 7, there is also an optimized range of the MH anode thickness in this prismatic model, based on the targeted energy density. For example, with a target of 200 Wh/kg, the MH anode thickness is optimally 2 – 2.5 mm. The inputs and results from an individual calculation for the contour plots of Fig. 7 are provided in Table S2 below. The input values in the EXAMPLE CASE column are

based on the specifications determined by Fig. S9 and our MH cycling data. For this example, an anode capacity of 400 mAh/g and thickness of 2.2 mm are chosen. The nominal cathode current is set to match the specifications of the MH anode with a discharge rate of $C/3$. The model then returns a specific energy density of 207 Wh/kg and a volumetric energy density of 427 Wh/L.

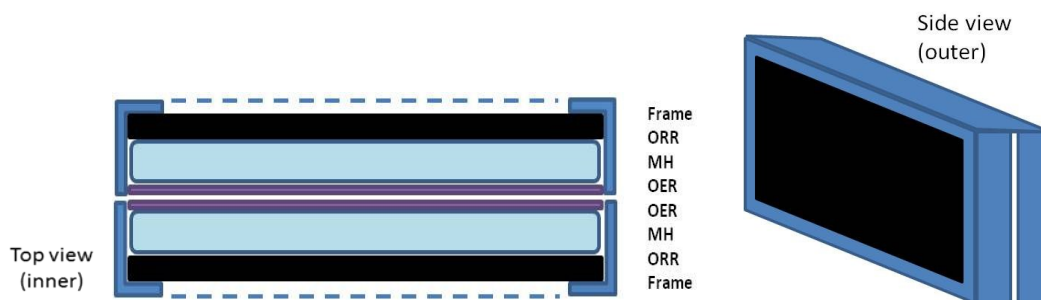


Figure S8. Top view (left) and 3D side view (right) drawings of the 100-Wh MH-air cell (dimensions not proportional).

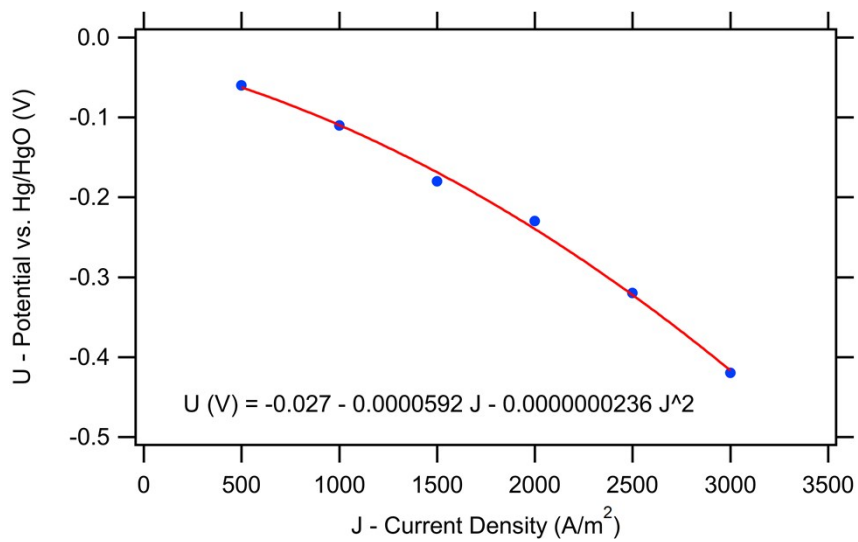


Figure S9: Plot of electrode potential versus current density for the air electrode manufactured by Electric Fuel.²

Table S2: Input values and energy density results for an example case of a 100 Wh MH-Air cell.

Table of Cell Parameters								
INPUTS			OUTPUTS			EXAMPLE CASE		
Cathode density	4.00E+03	kg/m ³	Cell width	2.02E-01	m	Cathode nominal current	1.30E+03	A/m ²
Anode density	4.00E+03	kg/m ³	Cell length	1.02E-01	m	Cathode nominal potential	-1.44E-01	V
KOH Density	1.25E+03	kg/m ³	Cell thickness w/o frame	9.30E-03	m	vs. Hg/HgO		
Plastic density	9.00E+02	kg/m ³	Cell thickness w/ frame	1.13E-02	m	Anode capacity	4.00E+02	Ah/kg
Stainless steel density	8.00E+03	kg/m ³	Frame area on air electrode	2.90E-03	m ²	Anode nominal potential	-8.50E-01	V
Aluminum density	2.70E+03	kg/m ³	Active area, 2 sides	3.42E-02	m ²	vs. Hg/HgO		
Nickel mesh density	2.50E+02	kg/m ³	Frame volume	1.15E-05	m ³	Anode thickness	2.20E-03	m
Cell Width	2.00E-01	m	Whole cell volume	2.33E-04	m ³	Cell nominal potential	7.06E-01	V
Cell Length	1.00E-01	m	Frame weight	1.03E-02	kg	Corresponding anode C-rate	3.16E-01	1/h
Frame width	5.00E-03	m	Cathode weight	8.00E-02	kg	Corresponding cell current	4.45E+01	A
Cathode thickness	5.00E-04	m	Anode weight	3.52E-01	kg	Cell Power	3.14E+01	W
Anode thickness	2.20E-03	m	Aux electrode weight	2.50E-03	kg	Cell theoretical capacity	1.41E+02	Ah
Aux electrode thickness	5.00E-04	m	Cell total weight w/o KOH	4.45E-01	kg	Cell nominal energy	9.94E+01	Wh
Separator thickness	1.20E-04	m	Cell total weight w/ KOH	4.81E-01	kg	Specific energy	2.07E+02	Wh/kg
Frame thickness	1.00E-03	m				Volumetric energy	4.27E+02	Wh/L
Flow chn thickness	2.92E-03	m						
Cooling thickness	5.00E-04	m						
KOH to MH mass ratio	2.05E-01	g/g						

- 1 Purushothaman, B. K. & Wainright, J. S. Analysis of Pressure Variations in a Low-Pressure Nickel-Hydrogen Battery– Part 2: Cells with Metal Hydride Storage. *J. Power Sources* **206**, 421-428, doi:10.1016/j.jpowsour.2012.01.149 (2012).
- 2 "Electric Fuel Air Electrodes" <http://electric-fuel.com/rd/zinc-air/air-electrode/> (2015).